Optical properties of the Einstein–de Sitter–Kasner universe

Sylvie Landry* and Charles C. Dyer†
Scarborough Campus, Department of Astronomy, University of Toronto, 1265 Military Trail, Scarborough, Ontario, Canada M1C 1A4
(Received 20 December 1996)

Most studies of gravitational lensing and their impact on observations concentrate on lensing structures which are bounded, that is, of some finite size in an otherwise reasonably smooth background universe. In this paper, we consider a model of the universe, the ''cheese slice'' universe, where the lensing is caused by very large scale structures: large slabs of alternating pure vacuum and Friedmann-Lemaître-Robertson-Walker (FLRW) dust. The ray tracing problem is solved and shows that only the Kasner regions will introduce a bending in the beam as it propagates. The Kasner slices also introduce anisotropic redshift effects. The optical scalar equations are used as a tool to obtain the cross-sectional area and shape of the beam. All physical properties of a bundle of rays traveling through the cheese slice model are obtained analytically. The only nonanalytical result is the evaluation, in Kasner regions, of the time variable along the beam as a function of the affine parameter. Practical model results are obtained from a computer code. Multislice models are studied and the resulting impact on astronomical observations, which includes the introduction of shear and amplification, is demonstrated. [S0556-2821(97)00918-1]

PACS number(s): 98.80.Hw

I. INTRODUCTION

While it is clear that the universe does not have an homogeneous matter distribution on most observable scales [1,2], we still have very limited models to describe the inhomogeneities observed. Most attention is given to ''clumps'' in the distribution, by which we mean spatially bounded or quasispherical concentrations of matter [3–11]. There is ample evidence for other structural classes, such as filaments, sheets, and quasispherical voids or underdense regions. It is difficult to incorporate some of these structures (particularly the sheet and filament components) in the conventional Friedmann-Lemaître-Robertson-Walker (FLRW) space-times and the usual perturbation schemes utilized to study inhomogeneous matter distributions.

Many recent observational results point to an observable large scale structure for the universe, which includes large void regions and significant layering in the distribution of visible matter as indicated by the distribution of galaxies and quasars. The study by Broadhurst *et al.* [12] shows apparent layering in the distribution of galaxies. Preferred redshifts in the distribution of quasars have been studied for many years, beginning with Burbidge and Burbidge [13], and confirmed by a number of later studies. Arp *et al.* [14] have demonstrated significant periodicity in the quasar redshift distribution looking in two principal directions of the sky. The periodicity they found extends out to redshifts as high as 3.47, with five or more cycles being evident.

A useful approach to developing models which include the more general structures discussed above is to consider models in which the universe has a lattice configuration. Such a construction would consist of three sets of mutually orthogonal thick slabs of matter, separated by regions of low density (vacuum regions in the simplest case). The range of structures includes large bounded voids, sheets, filaments (at the intersections of two orthogonal sheets), and quasispherical clumps (at the intersections of three mutually orthogonal sheets). As with any cosmological model, the lattice universe is a significant simplification of reality, but it could be expected to show some of the effects that one would expect in a more realistic, but more intractable representation.

The lattice models differ significantly from the FLRW models on scales comparable to the lattice distances, but on very large scales they would likewise obey an appropriately averaging cosmological principle, at least as it depends on the average density. In addition, the lattice models would appear anisotropic to a local observer, due to the optical effects that are dependent on the degree of alignment between a given line of sight and the principal axes of the sheets. In order to properly ascertain the observable properties of these models, which are significantly complicated by the optical effects mentioned above, a proper solution of the Einstein field equations is required to maintain consistency in the optical calculations.

Using the restriction to Newtonian gravity and a static universe, Lehle [15] has shown that there could be significant observable effects in such a lattice universe. However, because of the restrictions inherent to his approach, his work did not show some of the redshift effects discussed in this paper.

While the formalism for joining two different space-times is well developed [16], examples of its successful application are rare and highly nontrivial to obtain. Therefore, as a first step in studying models with the desired lattice structure, we consider the simpler case of a universe which has a multislice structure on a large scale and is constructed by alternating slices of Einstein–de Sitter dust and Kasner vacuum regions (see Fig. 1). Although the universe does not appear to have such a ''cheese slice'' structure, our model allows us to investigate the effects of very large inhomogeneities on the

*Present address: Département de Physique et Observatoire du Mont Mégantic, Université Laval, Ste-Foy, Québec, G1K 7P4, Canada. Electronic address: slandry@phy.ulaval.ca
†Electronic address: dyer@manitou.astro.utoronto.ca

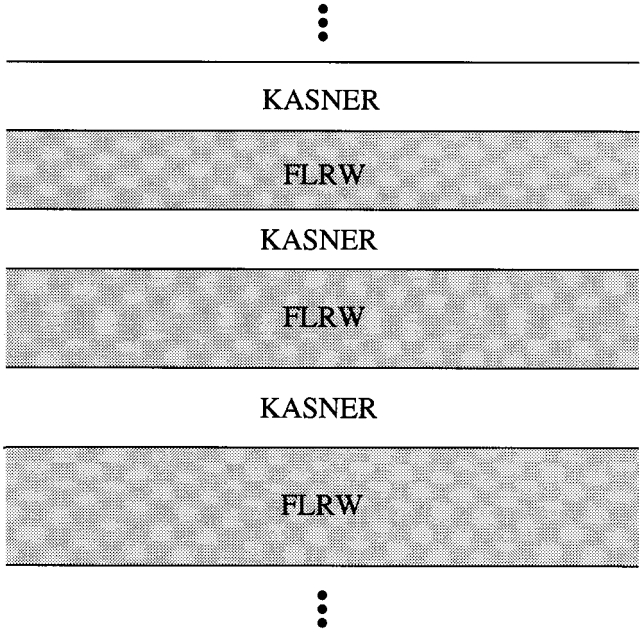

FIG. 1. Proposed model: the cheese slice universe.

propagation of a beam of light. The geometry of the cheese slice universes is tractable, since the system described yields an exact solution to the Einstein field equations, as discussed in Ref. [17].

The matching of FLRW space-times onto a Kasner vacuum region has been investigated in Ref. [17]. We have shown that only a spatially flat Einstein–de Sitter region can be joined smoothly to a special case of the Kasner space-time. We have also demonstrated that the pressure must vanish for the permanent matching to be possible. The metrics involved, in comoving cylindrically symmetric coordinates, are

$$ds^2 = dt^2 - a^2 t^{4/3}(dr^2 + r^2 d\phi^2 + dz^2) \tag{1}$$

in the Einstein–de Sitter region and

$$ds^2 = dT^2 - a^2 T^{4/3}(dr^2 + r^2 d\phi^2) - b^2 T^{-2/3} dZ^2 \tag{2}$$

in the Kasner region. Constants a and b are introduced to ensure proper unit bookkeeping. The two metrics are identical for surfaces with $z = Z = \text{const}$ and $t = T$. In the cheese slice cosmological model, the initial conditions of very thin and dense slices of matter in a vacuum background evolve into a universe almost entirely filled with cosmological dust with only thin slices of vacuum. In this paper, we shall use the optical scalar formalism to investigate the effects of such large inhomogeneities on the propagation of a beam of light. The propagation of a single light ray is studied in detail in the next section. In Sec. III, the cross-sectional area and shape of a beam of light traveling through our model are derived. Multislice models are investigated in Sec. IV, and the major conclusions are summarized in Sec. V.

II. RAY PROPAGATION

The propagation of a single light ray through the cheese slice model is the topic of this section. From now on, we will use the symbols F and K to designate indexed quantities or scalars associated with the FLRW and Kasner regions, respectively.[1]

The null tangent vector to the geodesics, $k^a = dx^a/d\tau \equiv \dot{x}^a$, can be obtained directly from the Euler-Lagrange equations

$$\frac{d}{d\tau}\frac{\partial L}{\partial \dot{x}^a} - \frac{\partial L}{\partial x^a} = 0, \tag{3}$$

where $L = (ds/d\tau)^2$ is the Lagrangian describing the gravitational field. The general form for the Lagrangian in Einstein–de Sitter space-time is

$$L_F = \dot{t}^2 - a^2 t^{4/3}(\dot{r}^2 + r^2\dot{\phi}^2 + \dot{z}^2). \tag{4}$$

Since we are free to orient our coordinate system so that $\phi = \text{const}$ and $d\phi = 0$, we can choose $k^2 \equiv d\phi/d\tau = 0$. The Lagrangian reduces to

$$L_F = \dot{t}^2 - a^2 t^{4/3}(\dot{r}^2 + \dot{z}^2), \tag{5}$$

and the null tangent vector is

$$k_F^0 = \varepsilon_t \frac{\xi}{t^{2/3}}, \quad k_F^1 = \varepsilon_r \frac{\xi\sqrt{\eta^2 - 1}}{\eta a t^{4/3}}, \quad \text{and} \quad k_F^3 = \varepsilon_z \frac{\xi}{\eta a t^{4/3}}, \tag{6}$$

where ξ and η are positive definite constants of integration. The sign of each component of k^a is carried through distinct indicators ε_t, ε_r, and ε_z which can take on one of two values ± 1. The actual value will be determined by the ''type'' of ray considered: time reversed ($\varepsilon_t = -1$, $\varepsilon_r = +1$, and $\varepsilon_z = -1$) or time forward ($\varepsilon_t = +1$, $\varepsilon_r = -1$, and $\varepsilon_z = +1$). When time-reversed (-forward) rays are considered, we are simply studying their behavior back (forward) into time.

In Kasner space-time, the general form for the Lagrangian is

$$L_K = \dot{T}^2 - a^2 T^{4/3}(\dot{r}^2 + r^2\dot{\phi}^2) - b^2 T^{-2/3}\dot{z}^2. \tag{7}$$

Again, symmetry considerations enable us to choose $k_K^2 \equiv k_K^\phi = 0$. L_K reduces to

$$L_K = \dot{T}^2 - a^2 T^{4/3}\dot{r}^2 - b^2 T^{-2/3}\dot{z}^2, \tag{8}$$

and the null tangent vector has the components

$$k_K^0 = \varepsilon_t T^{-2/3}\sqrt{\alpha^2 + \left(\frac{\gamma}{b}\right)^2 T^2}, \quad k_K^1 = \varepsilon_r \frac{\alpha}{a T^{4/3}},$$

and

$$k_K^3 = \varepsilon_z \frac{\gamma}{b^2} T^{2/3}, \tag{9}$$

[1]Throughout this paper Greek indices take the range 1–3 and Latin indices the range 0–3. The indices (0,1,2,3) correspond to (t, r, ϕ, z) or (T, r, ϕ, Z) depending on the metric used.

where α and γ are positive-definite constants of integration.

We need to determine how k^a crosses the boundary. We first consider a point comoving with the boundary surface separating the two regions. The observer's four-velocity and the null tangent vector to the geodesic must satisfy

$$(u_a k^a)_F=(u_a k^a)_K \quad \text{and} \quad (u_a u^a)_F=(u_a u^a)_K=1. \quad (10)$$

The first condition simply means that an observer fixed to a point measures the same frequency whether it is measured in the Einstein–de Sitter or Kasner space-times. The second equation requires that the observer be timelike in both frames. These conditions imply that *at the surface* $(k^0)_F=(k^0)_K$ (i.e., the time component of the null tangent vector is continuous across the boundary). Hence, relations (6) and (9) yield

$$\xi=\sqrt{\alpha^2+\left(\frac{\gamma}{b}\right)^2 t_{\rm in}^2}, \quad (11)$$

where $t_{\rm in}$ is the time evaluated at entry of the current Kasner slice.[2]

We now consider an observer moving on the interface, in the radial direction. The metric elements involved are the same on both sides of the boundary, and hence $(u_a)_F=(u_a)_K$. The condition that the frequency be continuous and $(k^0)_F=(k^0)_K$ requires that *at the surface* $(k^1)_F=(k^1)_K$. From Eqs. (6), (9), and (11) we can write

$$\alpha=\xi\frac{\sqrt{\eta^2-1}}{\eta} \quad \text{and} \quad \frac{\gamma t_{\rm in}}{b}=\frac{\xi}{\eta}. \quad (12)$$

The null tangent vector then has components

$$k_K^0=\varepsilon_t\frac{\xi}{\eta T^{2/3}}\sqrt{(\eta^2-1)+\left(\frac{T}{t_{\rm in}}\right)^2},$$

$$k_K^1=\varepsilon_r\frac{\xi\sqrt{\eta^2-1}}{\eta a T^{4/3}}, \quad \text{and} \quad k_K^3=\varepsilon_z\frac{\xi T^{2/3}}{\eta b t_{\rm in}}. \quad (13)$$

Finally, the physical symmetries of the model and the fact that k^a is a null vector suggest that k^3 is not continuous across the boundary but $g_{33}k^3k^3$ is continuous.

A. Bending angle

We define Ψ as the angle between a three-vector normal to the boundary surface $\vec{V}$, and the tangent three-vector to the geodesic $\vec{k}$. Ψ can easily be calculated from the familiar equation for scalar products $\vec{V}\cdot\vec{k}=|\vec{V}||\vec{k}|\cos\Psi$. Since k^a is a null vector, g_{ab} is diagonal, and $\vec{V}$ is normal to the boundary, we have $\cos\Psi=-|g_{33}|^{1/2}(k^3/k^0)$ and $\sin\Psi=|g_{11}|^{1/2}(k^1/k^0)$, which yields

[2]Since at each interface $T=t$, we will use $t_{\rm in}$ ($t_{\rm out}$) as the time evaluated at entry (exit) of the current slice.

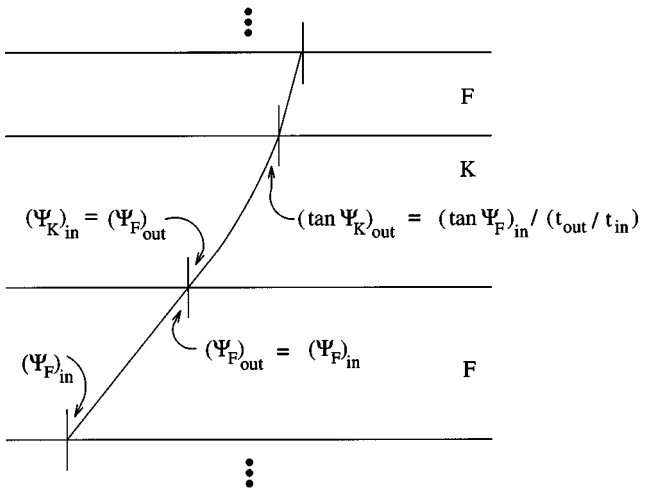

FIG. 2. Time-forward ray propagating through the cheese slice universe.

$$\tan\Psi=-\left(\frac{|g_{11}|}{|g_{33}|}\right)^{1/2}\frac{k^1}{k^3}. \quad (14)$$

Through the Einstein–de Sitter line element, Eq. (1), and relations (6) and (14), we obtain

$$\tan\Psi_F=\sqrt{\eta^2-1}\equiv\text{const}. \quad (15)$$

This result was expected since the Einstein–de Sitter space-time is homogeneous and isotropic. Similarly, Eqs. (2), (13), and (14) enable us to write, for the Kasner region

$$\tan\Psi_K=\frac{\sqrt{\eta^2-1}}{(T/t_{\rm in})}=\frac{\tan\Psi_F}{(T/t_{\rm in})}, \quad (16)$$

where Ψ_F was evaluated in the *previous Einstein–de Sitter slice*. At the crossing of the boundary into the Kasner region, no bending will occur at the surface. As a time-forward (-reversed) ray propagates through the Kasner slice, it will be forced to move towards (away from) the normal to the surface separating the two regions (see Fig. 2).

We now substitute relation (15) into Eqs. (6) and (13) and write the null tangent vector in its final form

$$k_F^0=\varepsilon_t\frac{\xi}{t^{2/3}}, \quad k_F^1=\varepsilon_r\frac{\xi\sin\Psi_{\rm in}}{at^{4/3}}, \quad \text{and} \quad k_F^3=\varepsilon_z\frac{\xi\cos\Psi_{\rm in}}{at^{4/3}} \quad (17)$$

and

$$k_K^0=\varepsilon_t\frac{\xi\cos\Psi_{\rm in}}{T^{2/3}}\sqrt{\tan^2\Psi_{\rm in}+\left(\frac{T}{t_{\rm in}}\right)^2},$$

$$k_K^1=\varepsilon_r\frac{\xi\sin\Psi_{\rm in}}{aT^{4/3}}, \quad \text{and} \quad k_K^3=\varepsilon_z\frac{\xi T^{2/3}\cos\Psi_{\rm in}}{bt_{\rm in}} \quad (18)$$

for Einstein–de Sitter and Kasner slices, respectively.

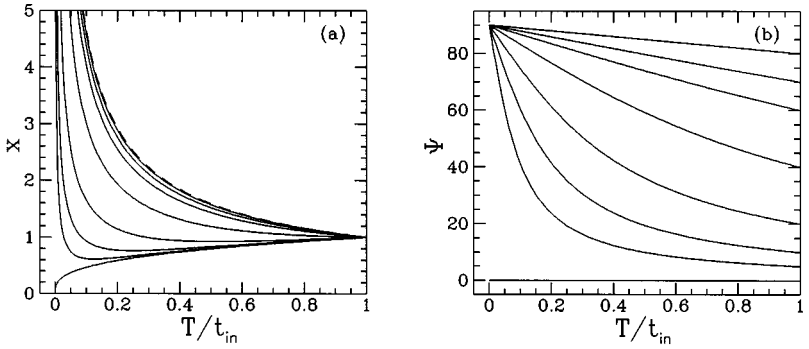

FIG. 3. Kasner slice: x and Ψ (in degrees) evaluated using $\Psi_{in}=0°$ (bottom curve), 5°, 10°, 20°, 40°, 60°, 70°, and 80° (top solid line). The dashed line represents the redshift contribution from an Einstein–de Sitter slice.

The distance traveled by the central ray in the radial and z directions as a function of time along the beam can be computed by integrating dr/dt, dz/dt, dr/dT, and dZ/dT. In Einstein–de Sitter space-time, the two equations of interest are

$$a(r-r_{in})_F=-3t_{in}^{1/3}\sin\Psi_{in}\left\{\left(\frac{t}{t_{in}}\right)^{1/3}-1\right\} \tag{19}$$

and

$$a(z-z_{in})_F=3t_{in}^{1/3}\cos\Psi_{in}\left\{\left(\frac{t}{t_{in}}\right)^{1/3}-1\right\}, \tag{20}$$

where, as previously defined, the subscript ''in'' designates the value taken by a given variable at entry of the current slice. In Kasner regions, we must numerically integrate the equations

$$a(r-r_{in})_K=-t_{in}^{1/3}\tan\Psi_{in}\int_{t_{in}}^{T}\frac{d(T/t_{in})}{(T/t_{in})^{2/3}\sqrt{\tan^2\Psi_{in}+(T/t_{in})^2}} \tag{21}$$

and

$$b(Z-Z_{in})_K=t_{in}^{4/3}\int_{t_{in}}^{T}\frac{(T/t_{in})^{4/3}d(T/t_{in})}{\sqrt{\tan^2\Psi_{in}+(T/t_{in})^2}}. \tag{22}$$

A Simpson rule integrator is used to perform these integrations.

B. Redshift factor

An observer with four-velocity u^a observes a photon with null tangent vector k^a to have a frequency proportional to $u_a k^a$. Hence, the redshift factor across a slice, that is, the ratio of observed frequencies, for a time-reversed ray can be written as $x\equiv 1+$ redshift $=(u_a k^a)_{out}/(u_a k^a)_{in}$. Since the boundaries are comoving surfaces in both regions, we have

$$x_F=\left(\frac{t_{in}}{t_{out}}\right)^{2/3}, \tag{23}$$

$$x_K=\frac{\cos\Psi_{in}\sqrt{\tan^2\Psi_{in}+(t_{out}/t_{in})^2}}{(t_{out}/t_{in})^{2/3}} \tag{24}$$

for the Einstein–de Sitter and Kasner regions, respectively. Time-reversed rays [i.e., rays for which $(t_{out}/t_{in})<1$] will experience the usual redshift effect each time an Einstein–de Sitter slice is crossed.

The contribution of each Kasner region, for different Ψ_{in} values, as a function of (T/t_{in}) is illustrated in Fig. 3(a). The minimum point of x_K can be found by setting $dx_K/d(T/t_{in})=0$. When $(T/t_{in})=\sqrt{2}\tan\Psi_{in}$, the contribution of the Kasner region to the redshift factor will have reached its lowest numerical value. Substituting this result into relation (16) we find that the turnover point is at $\Psi_K\simeq 35°$. When traveling through a Kasner slice, the rays will be blueshifted as long as $\Psi_K\lesssim 35°$. If $\Psi_K\gtrsim 35°$, then the expansion along the radial coordinate dominates the contraction along z and the rays will be redshifted. Since Ψ is a function of the thickness of the slice and its value at entry, the net contribution of a Kasner slice may be a redshift or a blueshift effect.

The behavior of Ψ as a function of (T/t_{in}) as the beam moves across a Kasner slice is illustrated in Fig. 3(b). For all rays with $\Psi_{in}\neq 0$ the final value for the bending angle (when $T/t_{in}=0$) is $\Psi=90°$. This outcome is inevitable however small the initial tilt. This striking degeneracy between rays with $\Psi_{in}=0$ and those with $\Psi_{in}\neq 0$ will cause drastic differences when computing the characteristics of the beam.

Finally, the redshift factor for the entire model is the product of each contribution.

C. Matching k^a at subsequent interfaces

It was shown in Dyer, Landry, and Shaver [17] that for the matching between an Einstein–de Sitter region and a Kasner region to be permanent, the only components of g_{ab} that need be continuous at the boundary surface are g_{00}, g_{11}, and g_{22}. We have shown in this section that k^0, k^1, and the product $g_{33}k^3k^3$ must also be continuous—we stress the fact that g_{33} and k^{33} *are not* individually continuous at the boundary. We must ensure that the continuity of all previous variables is preserved at each subsequent interface.

We will use circled numerical indices to specify at which interface a given quantity is evaluated. At the second boundary surface, the junction of a Kasner slice and an Einstein–de Sitter slice, the continuity of k^0 requires that

$$\xi_{②}=\xi_{①}\cos\Psi_{①}\sqrt{\tan^2\Psi_{①}+(t_{②}/t_{①})^2}, \tag{25}$$

whereas the continuity of k^1 implies

$$\xi_{①}\sin\Psi_{①}=\xi_{②}\sin\Psi_{②}, \tag{26}$$

from which

$$\sin\Psi_{②}=\frac{\tan\Psi_{①}}{\sqrt{\tan^2\Psi_{①}+(t_{②}/t_{①})^2}} \tag{27}$$

is obtained. This result is equivalent to the bending relation described by Eq. (16). In addition, the product $g_{33}k^3k^3$ is found to be identically matched.

On the third boundary, all quantities of interest are continuous if $\xi_{②}$ is used as the constant of integration for $(k^0_K)_{③}$. At the fourth interface, a new value for ξ will have to be computed, and so on. When a light ray crosses a Kasner–Einstein–de Sitter boundary, the constant ξ must be computed using the recursion relation

$$\xi_{ⓘ}=\xi_{-ⓘ}\cos\Psi_{-ⓘ}\sqrt{\tan^2\Psi_{-ⓘ}+(t_{ⓘ}/t_{-ⓘ})^2}, \tag{28}$$

where the subscripts ⓘ and $-ⓘ$ designate quantities evaluated at the current and previous interfaces, respectively. The bending angle used at entry of each new slice is obtained from relations (15) and (16).

III. SHAPE AND SIZE OF THE BEAM

In the geometrical optics approximation, the optical scalar equations (OSE's) describe the evolution of the cross section of an infinitesimal beam as the photons propagate. The Ehlers-Sachs theorem [18] states that the cross section of an irrotational congruence of null geodesics is expanded and sheared at the respective rates

$$\Theta=\frac{1}{2}k^a_{\|a}\quad\text{and}\quad|\sigma|=\left(\frac{1}{2}k_{(a\|b)}k^{a\|b}-\Theta^2\right)^{1/2}, \tag{29}$$

with respect to the affine parameter τ along the beam. $\|a$ denotes covariant differentiation with respect to x^a, and () represents symmetrization over the enclosed indices. The only effect of Θ is to rescale the area, and thus it is expected to be real. Since σ is characterized by an amplitude and an orientation, it is a complex quantity.

The optical scalars Θ and σ are propagated along the null geodesics according to the OSE's [18]

$$\dot\Theta+\Theta^2+\sigma\overline{\sigma}=\mathcal{R}=\tfrac{1}{2}R_{ab}k^ak^b, \tag{30}$$

$$\dot\sigma+2\Theta\sigma=\mathcal{F}e^{i\beta}=C_{aibj}k^ak^b\overline{s^i s^j}, \tag{31}$$

where the dot is equivalent to $d/d\tau$, the bar denotes complex conjugation, R_{ab} is the Ricci curvature tensor, and C_{aibj} is the Weyl curvature tensor. s^i is a complex null vector parallelly propagated along the congruence and satisfies the tetrad conditions $s^ak_a=0$ and $s^a\overline{s_a}=-1$ (for -2 signature). The Ricci driving term $\mathcal{R}$ represents focusing due to matter enclosed by the beam and is always nonpositive for positive-definite local energy density, whereas the Weyl driving term $\mathcal{F}e^{i\beta}$ represents focusing by nonlocal matter.

Kantowski [19] derived the relationship between the optical scalars and the curvature structure of the wavefront defined by the intersection of the observer's rest frame with a specific null hypersurface. We define the real quantities $C_{\mp}$ and $\alpha_{\mp}$ in terms of the two principal curvatures of the wavefront:

$$\Theta\pm\sigma=\frac{d[\ln(C_{\mp}e^{i\alpha_{\mp}})]}{d\tau}. \tag{32}$$

We can now write Eqs. (30) and (31) as

$$\ddot C_{\mp}/C_{\mp}+\dot\alpha^2=\mathcal{R}\pm\mathcal{F}\cos\beta \tag{33}$$

and

$$\ddot\alpha+\dot\alpha(\dot C_{+}/C_{+}+\dot C_{-}/C_{-})=-\mathcal{F}\sin\beta. \tag{34}$$

If A is the cross-sectional area of the beam, then $\Theta=\dot A/(2A)$. Hence A is proportional to $C_{+}C_{-}$, and the distortion factor is proportional to C_{+}/C_{-}. This form of the OSE is very useful in situations where space-times with much symmetry are involved.

The Einstein–de Sitter space-time is conformally flat, that is, $C_{aibj}=0$ everywhere, and therefore $\mathcal{F}e^{i\beta}=0$. The remaining driving term, computed through $\mathcal{R}_F=(1/2)R_{ab}k^ak^b$, is easily obtained since the only nonzero components of the Ricci tensor are R_{00}, R_{11}, R_{22}, and R_{33}. The Ricci driving term then reduces to

$$\mathcal{R}_F=\frac{1}{2}(R_{00}k^0k^0+R_{11}k^1k^1+R_{33}k^3k^3)=\frac{-2\xi^2}{3t^{10/3}}. \tag{35}$$

The Kasner space-time is a vacuum solution of the Einstein field equations, and hence $\mathcal{R}_K=0$. Following Dyer [20] one may use spinor formalism to determine $\overline{s^i}$. At any point, k^a defines a one-spinor K^A, up to a phase factor, through [21]

$$K^B\overline{K^{\dot X}}=\pm\sigma_a^{B\dot X}k^a, \tag{36}$$

where $\sigma_a^{B\dot X}$ are the spinor connections.[3] For the purpose of finding the Weyl driving term, we will consider time-forward null tangent vectors. Hence, the ''+'' sign in Eq. (36) will be chosen. Since k^a is real, $k^2=0$, and $\sigma_2^{B\dot X}$ is the only complex spin connection matrix, it follows that $K^B\overline{K^{\dot X}}$ must be real. Hence, K^1 and K^2 must have the same phase factor. In order to establish a basis for spinors, we introduce a second one-spinor μ_A such that $K^A\mu_A=1$, and then define the complex null vector $s^a=\sigma^a_{B\dot X}K^B\overline{\mu^{\dot X}}$. The parallel propagation of k^a and s^a along the geodesic requires that K^B and μ^B must

[3]Capital Latin letters take the values 1 and 2.

also be parallel propagated. We may choose K^A to be real without losing generality on k^a. From Eqs. (18) and (36) we finally obtain

$$K^1=\frac{1}{2^{1/4}}\Upsilon_+ \quad \text{and} \quad K^2=\frac{1}{2^{1/4}}\Upsilon_-, \tag{37}$$

where $\Upsilon_\pm=\{k_K^0\pm bT^{-1/3}k_K^3\}^{1/2}$.

Because of cylindrical symmetry, we expect that, at a given time, the Weyl driving term should be independent of the radial coordinate r. The nonzero components of the Weyl tensor are C_{0101}, C_{0202}, C_{0303}, C_{1212}, C_{1313}, and C_{2323}. This enables us to write

$$\overline{s^0}=\frac{aT^{2/3}}{2}(g+h)\ ,\ \overline{s^2}=\frac{\overline{f}}{r},\ \text{and}\ \overline{s^3}=\frac{aT}{2b}(g-h), \tag{38}$$

where $g\equiv(K^1/K^2)(\overline{s^1}-i\,\overline{f})$, $h\equiv(K^2/K^1)(\overline{s^1}+i\,\overline{f})$, and $\overline{f}$ is an unknown function of T. Hence, it follows that $C_{aibj}k^ak^b\,\overline{t^i\,t^j}\propto\overline{f\,f}/T^2$. Finally, the normalization condition $K^A\mu_A=1$ enable us to write the Weyl driving term as

$$\mathcal{F}e^{i\beta}=C_{aibj}k^ak^b\,\overline{s^i\,s^j}=\frac{2\xi^2\sin^2\Psi_{\text{in}}}{3T^{10/3}} \tag{39}$$

up to a constant phase factor (i.e., $\beta=\text{const}$).

A. Principal curvatures: Solutions

The expansion and shearing rates undergone by a beam of light traveling through an Einstein–de Sitter slice once shearing effects have been introduced (i.e., when the slice of interest is not the observer's slice) can be computed via Eqs. (17) and (29):

$$\Theta_F=\varepsilon_t\xi\left(\frac{2}{3t^{5/3}}-\frac{\sin\Psi_{\text{in}}}{2art^{4/3}}\right) \tag{40}$$

and

$$|\sigma|_F=\frac{\varepsilon_r\xi\sin\Psi_{\text{in}}}{2art^{4/3}}. \tag{41}$$

One can easily verify that Eqs. (30) and (31) are satisfied, and that the phase factor of $\sigma\equiv|\sigma|e^{i\omega}$ is a constant (i.e., $\dot{\omega}_F=0$).

Similarly, in Kasner regions, Θ_K and $|\sigma|_K$ may be computed through relations (18) and (29):

$$\Theta_K=\varepsilon_t\xi\left(\frac{\cos\Psi_{\text{in}}(\tan^2\Psi_{\text{in}}+4(T/t_{\text{in}})^2)}{6T^{5/3}\sqrt{\tan^2\Psi_{\text{in}}+(T/t_{\text{in}})^2}}-\frac{\sin\Psi_{\text{in}}}{2arT^{4/3}}\right) \tag{42}$$

and

$$|\sigma|_K=\varepsilon_r\xi\sin\Psi_{\text{in}}\left(\frac{1}{2arT^{4/3}}-\frac{\tan\Psi_{\text{in}}}{2T^{5/3}\sqrt{\tan^2\Psi_{\text{in}}+(T/t_{\text{in}})^2}}\right). \tag{43}$$

The real part of Eq. (31) is satisfied if $\cos(\beta-\omega_K)=-1$, and so we can choose $\beta-\omega_K=\pi$. Since $\beta=\text{const}$, ω_K is also a constant.

We are then free to choose, in both space-times, σ to be real initially. We will define $\omega=0$, which implies $\beta=\pi$ and $\dot{\alpha}=0$.[4] Equation (34) is then identically satisfied. Since $\mathcal{R}_F$ and $\mathcal{F}_K$ are both simple functions of time coordinate, it is more suitable to use t (or T), instead of the affine parameter, as the independent variable. Relation (33) is then reduced to the decoupled pair

$$k^0k^0C_\mp''+k^0(k^0)'C_\mp'=(\mathcal{R}\mp\mathcal{F})C_\mp, \tag{44}$$

where the prime denotes total differentiation with respect to t (or T). We can also rewrite relation (32) in the simpler form

$$\Theta\pm|\sigma|=\frac{k^0C_\mp'}{C_\mp}. \tag{45}$$

1. Observer's slice

We now consider a conical beam of light with vertex at the observer and its base on the source of interest, so that A vanishes at the observer. In addition, the radial coordinate of the central ray evaluated at the vertex of the cone is, by definition, $r_{\text{obs}}\equiv0$. Therefore, it is inappropriate to use relation (45) in order to determine solutions for the principal curvatures in the observer's slice. Instead, we will solve Eq. (44) directly in the initial slice.

In Einstein–de Sitter space-time, Eq. (44) becomes

$$3t^2C_\mp''-2tC_\mp'+2C_\mp=0. \tag{46}$$

Since the space-time is homogeneous and isotropic, we are free to choose $C_+=C_-\equiv C$ initially. The general solution is $C=a_1t^{2/3}+a_2t$ and $A\propto C^2$. For small redshift [20],[5] $A\simeq(x-1)^2/2$ which enables us to find the constants of integration, and the cross-sectional area of the beam is

$$A_F=2\left[\left(\frac{t}{t_{\text{obs}}}\right)^{2/3}-\left(\frac{t}{t_{\text{obs}}}\right)\right]^2, \tag{47}$$

where t_{obs} is the time variable evaluated at the observer or, if expressed as a function of redshift factor,

[4]Note that in an Einstein–de Sitter slice β is irrelevant since $\mathcal{F}e^{i\beta}=0$.

[5]The cross-sectional area used throughout this paper has been rescaled in order to eliminate the solid angle $\Delta\Omega_{\text{obs}}$ at the observer: $A\equiv D_<^2/2$, where $D_<$ is the angular size distance.

$$A_F = 2x^{-5/2}[x^{1/4} - x^{-1/4}]^2. \tag{48}$$

The peak value of A is reached when $(t/t_{\rm obs}) = 8/27 \simeq 0.296$ or at redshift 1.25 ($x = 2.25$).

In Kasner space-time, Eq. (44) becomes

$$3u^2(\tan^2\Psi_{\rm obs} + u^2)C_{\mp}^{**} + u(-2\tan^2\Psi_{\rm obs} + u^2)C_{\mp}^{*} \pm 2\tan^2\Psi_{\rm obs} C_{\mp} = 0, \tag{49}$$

where the asterisk denotes total differentiation with respect to $u \equiv T/t_{\rm obs}$. The anisotropic nature of the vacuum region suggests that the importance of the axis of symmetry cannot be ignored. Consequently, if the first slice is to be represented by the Kasner metric, both C_+ and C_- will be needed to compute A.

Once a particular solution to Eq. (49) is known, further solutions can be obtained from a differential equation of lower order (see, for example, Ref. [22]). A particular solution for $(C_+)_K$ is

$$C_{+1} \propto u^{-1/3} \times \sqrt{\tan^2\Psi_{\rm obs} + u^2} \equiv Y_1(u). \tag{50}$$

A second particular solution can be found via $C_{+2} \propto v(u)Y_1(u)$, where $v(u)$ is a solution to $v^* \propto u^{4/3}/(\tan^2\Psi_{\rm obs} + u^2)^{3/2}$ giving $v \propto (ar)_K + Y_1^{-1} \times {\rm const}$, where $(ar)_K$ is described by Eq. (21). Since both particular solutions are linearly independent on the domain of interest, the general solution for C_+ is

$$(C_+)_K = a_1 Y_1(u) + a_2[(ar)_K Y_1(u) + 3t_{\rm obs}^{1/3}\tan\Psi_{\rm obs}], \tag{51}$$

where a_1 and a_2 are constants of integration.

Similarly, a particular solution to C_- is $\overline{C}_{-1} \propto u^{2/3}(ar)_K$, which yields $C_{-2} \propto \overline{v}(u)u^{2/3}(ar)_K$ where $\overline{v}(u)$ is a solution to $\overline{v}^*(u) \propto 1/(u^{2/3}(ar)_K^2\sqrt{\tan^2\Psi_{\rm obs} + u^2})$, from which $\overline{v} \propto (ar)_K^{-1} + {\rm const}$ is obtained. The general solution for C_- is

$$(C_-)_K = a_1^* u^{2/3}(ar)_K + a_2^* u^{2/3}, \tag{52}$$

where a_1^* and a_2^* are constants of integration.

If $A_K = (C_+)_K(C_-)_K$ is to be a viable solution in the first slice, we must require that both principal curvatures vanish at the observer. This requirement is easily met if $a_2 = -a_1/(3t_{\rm obs}^{1/3}\sin\Psi_{\rm obs}) \equiv a_1 \times P_0$ and $a_2^* = 0$, since $u|_{\rm obs} \equiv (T/t_{\rm obs})|_{\rm obs} = 1$ and $(ar)_K|_{\rm obs} = 0$. $(C_+)_K$ and $(C_-)_K$ then reduce to

$$(C_+)_K = a_1\left\{ Y_1(u)[1 + P_0(ar)_K] - \frac{1}{\cos\Psi_{\rm obs}} \right\} \tag{53}$$

and

$$(C_-)_K = a_1^* u^{2/3}(ar)_K. \tag{54}$$

The cross-sectional area of the beam is then

$$A_K = P_1 u^{2/3}(ar)_K\left[Y_1(u)[1 + P_0(ar)_K] - \frac{1}{\cos\Psi_{\rm obs}} \right], \tag{55}$$

where P_1 is a constant yet to be determined and $P_0 \equiv -1/(3t_{\rm obs}^{1/3}\sin\Psi_{\rm obs})$. In order for A_K to be a solution to $\Theta = (dA/d\tau)/(2A)$, it must reduce to $A_K \propto u^{2/3}(ar)_K Y_1(u)$, which can only be accomplished if $(C_+)_K|_{\rm obs} \neq 0$. Since there is no locally isotropic scale in Kasner space-time (i.e., shearing effects can never be ignored), a bundle of rays will never focus back to a point if it is solely traveling in that space-time. Thus no beam of interest can be ''launched'' in a Kasner region.

2. Subsequent slices

Once the beam has been properly launched in an Einstein–de Sitter region, that is, when the apex of the cone is at a caustic point (i.e., $A = 0$), we are free to integrate Eq. (45) in order to determine the principal curvatures of a beam traveling in the remaining slabs of the cheese slice model.

The tangential extent of a beam traveling in the Einstein–de Sitter space-time can be independently obtained through the line element described by Eq. (1): $l_{\rm tg} = at^{2/3} r\,\delta\phi$, where $\delta\phi$ is the beam opening angle projected along the tangential direction[6] or

$$\frac{dl_{\rm tg}/dt}{l_{\rm tg}} = \frac{2}{3t} + \frac{\varepsilon_r \sin\Psi_{\rm in}}{\varepsilon_t a r t^{2/3}} = \frac{2}{3t} - \frac{\sin\Psi_{\rm in}}{a r t^{2/3}}. \tag{56}$$

We now substitute Eqs. (40) and (41) and $k_F^0 = \varepsilon_t \xi/t^{2/3}$ into Eq. (45), giving

$$\left(\frac{dC_-/dt}{C_-}\right)_F = \frac{2}{3t} - \frac{\sin\Psi_{\rm in}}{a r t^{2/3}} \tag{57}$$

and

$$\left(\frac{dC_+/dt}{C_+}\right)_F = \frac{2}{3t}. \tag{58}$$

A straightforward comparison between relations (56) and (57) yields $(C_-)_F = l_{\rm tg} \propto r t^{2/3}$. Since Einstein–de Sitter space-time has $\mathcal{F} = 0$, the real part of Eq. (31) reduces to $(|\sigma|A)_F \propto (|\sigma|_F C_+ C_-)_F = {\rm const}$, from which $(C_+)_F \propto t^{2/3}$ is obtained.

We stress the fact that $|\sigma|$ is the *amplitude* of the shearing rate and it is not, in our case, a positive-definite function. The biperiodicity property of the phase factor of σ forces us to choose the proper sign by requiring the correspondence between $l_{\rm tg}$ and C_- to be consistent in both time directions.

---

[6] $l_{\rm tg}$ is tangential to the axis of symmetry and lies in a plane perpendicular to it.

Finally, a convenient normalization of C_+ and C_- with respect to output values from the previous Kasner slice yields

$$(C_-)_F=(C_-)_{\rm in}\left(\frac{t}{t_{\rm in}}\right)^{2/3}\left(\frac{r}{r_{\rm in}}\right)$$

and

$$(C_+)_F=(C_+)_{\rm in}\left(\frac{t}{t_{\rm in}}\right)^{2/3}, \tag{59}$$

where the index ''in'' denotes variables evaluated at the entrance of the current Einstein–de Sitter slice (i.e., exit values from previous Kasner slice).

In Kasner space-time, we expect $(C_-)_K$ to behave the same way as $(C_-)_F$ since the metrics in both regions of interest have the same expansion factor when $dz=dZ=0$. This assumption is easily verified through

$$\left(\frac{dl_{\rm tg}/dT}{l_{\rm tg}}\right)_K=\frac{2}{3T}-\frac{\tan\Psi_{\rm in}}{arT^{2/3}\sqrt{\tan^2\Psi_{\rm in}+(T/t_{\rm in})^2}}$$
$$=\left(\frac{dC_-/dT}{C_-}\right)_K, \tag{60}$$

which confirms that $(C_-)_K=l_{\rm tg}\propto rT^{2/3}$. $(C_+)_K$ can be obtained by solving the first-order differential equation

$$\left(\frac{dC_+/dT}{C_+}\right)_K=\frac{(T/t_{\rm in})^2-\tan^2\Psi_{\rm in}}{2T\{\tan^2\Psi_{\rm in}+(T/t_{\rm in})^2\}}+\frac{1}{6T}, \tag{61}$$

with $\ln C_+\propto(1/6)\ln\{(v+\tan^2\Psi_{\rm in})^3/v\}$ as its solution, where $v\equiv(T/t_{\rm in})^2$. Once again, we normalize C_+ and C_- with respect to output values from the previous Einstein–de Sitter slice, and we finally obtain

$$(C_-)_K=(C_-)_{\rm in}\left(\frac{T}{t_{\rm in}}\right)^{2/3}\left(\frac{r}{r_{\rm in}}\right) \tag{62}$$

and

$$(C_+)_K=(C_+)_{\rm in}\cos\Psi_{\rm in}\frac{\sqrt{\tan^2\Psi_{\rm in}+(T/t_{\rm in})^2}}{(T/t_{\rm in})^{1/3}}. \tag{63}$$

3. Degenerate case: $\Psi=0$

If the tilt angle at the observer vanishes, then the beam will remain parallel to the axis of symmetry as it is propagated through the cheese slice model, consistent with Eqs. (15) and (16). Since $r_{\rm obs}=0$, the radial coordinate of the central ray will remain $r=0$ and $dr/d\tau\equiv k^1=0$.

For this special case only, the null tangent vector in Einstein–de Sitter regions has components

$$k^0_F=\varepsilon_t\frac{\xi}{t^{2/3}},\quad k^1_F=k^2_F=0,\quad k^3_F=\varepsilon_z\frac{\xi}{at^{4/3}}, \tag{64}$$

and the expansion and shearing rates reduce to

$$\Theta_F=\varepsilon_t\frac{2\xi}{3t^{5/3}}\ \text{ and }\ |\sigma|^2_F=0. \tag{65}$$

The central ray is traveling solely in the z direction, and hence there will be no distortion of the cross-sectional area of the beam. Since the Ricci driving term is due to matter enclosed in the beam, it is still described by Eq. (35).

Similarly, in Kasner space-time, k^a becomes

$$k^0_K=\varepsilon_t\frac{\xi T^{1/3}}{t_{\rm in}},\quad k^1_K=k^2_K=0,\quad k^3_K=\varepsilon_z\frac{\xi T^{2/3}}{bt_{\rm in}}, \tag{66}$$

and the optical scalars reduce to

$$\Theta_K=\varepsilon_t\frac{2\xi}{3t_{\rm in}T^{2/3}}\ \text{ and }\ |\sigma|^2_K=0. \tag{67}$$

Again there will be no distortion of the beam area; only an expansion will occur, consistent with $\mathcal{F}=0$ for $\Psi_{\rm in}=0$, from Eq. (39).

In both regions of interest, the dimensions of the beam can be obtained through relation (45):

$$C\equiv C_+=(C_+)_{\rm in}\left(\frac{\rm time}{t_{\rm in}}\right)^{2/3}, \tag{68}$$

and $A\propto C_+^2$. The only relevant principal curvature is C_+, which is proportional to the diameter of the beam in the radial direction. Clearly, if a bundle of rays has a circular cross section, it will remain circular if and only if $\Psi_{\rm obs}=0$.

Finally, even though the principal curvature is described by relation (68) in both space-times, the time ratio is computed through two distinct equations. In Einstein–de Sitter regions, the ratio is obtained via

$$\left(\frac{t}{t_{\rm in}}\right)_F=\left(\frac{a(z-z_{\rm in})_F}{3t_{\rm in}^{1/3}\cos\Psi_{\rm in}}+1\right)^3, \tag{69}$$

where $\Psi_{\rm in}=\Psi_{\rm obs}=0$, while

$$\left(\frac{T}{t_{\rm in}}\right)_K=\left[\frac{4b(Z-Z_{\rm in})_K}{3t_{\rm in}^{4/3}}+1\right]^{3/4} \tag{70}$$

must be used in Kasner regions.

B. First three slices

We now investigate the changes in key properties of a beam as it travels through (1) a two-slice model constructed with a Kasner region much larger than the observer's slice

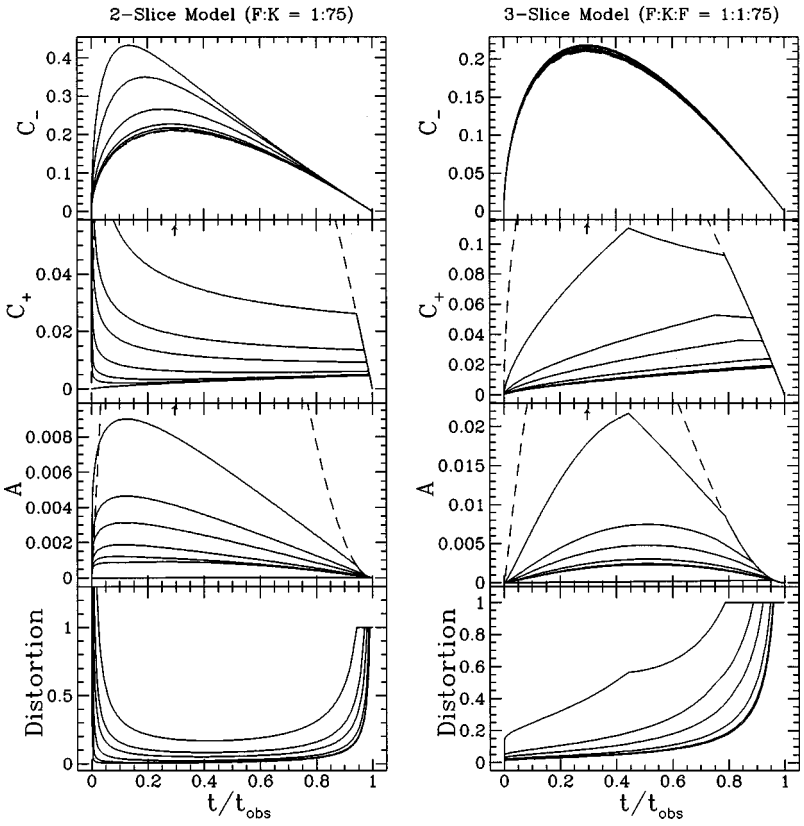

FIG. 4. Two- and three-slice models: When pertinent, a dashed line representing the variable of interest evaluated in the Einstein–de Sitter universe was included as a reference, and $t/t_{\rm obs}$ at peak value of C_+ and A in the reference model is indicated with an arrow. C_+ and A were evaluated using $\Psi_{\rm obs}=0°$ (bottom line), 10°, 20°, 40°, 60°, 70°, and 80° (top line). C_- and C_+/C_- were evaluated using $\Psi_{\rm obs}=10°$ (top line for C_- and bottom line for C_+/C_-) to 80° (bottom line for C_- and top line for C_+/C_-). C_+ graph in three-slice model: the curves for which $\Psi_{\rm obs}=0°$ and $\Psi_{\rm obs}=10°$ are overlapping and undistinguishable.

and (2) a three-slice model where the third slab, an Einstein–de Sitter region, is much larger than the two previous slices.

1. Two-slice model

The purpose of this special model is to isolate the effect of the Kasner space-time on the characteristics of the beam and compare the results with those obtained via the reference model: the Einstein–de Sitter cosmological model. We have chosen the relative ''thicknesses'' of the two slabs to be in the proportion $F{:}K=1{:}75$ [i.e., the quotient $a(z_{\rm out}-z_{\rm in})_F/b(Z_{\rm out}-Z_{\rm in})_K$ is in the ratio 1/75], where the vacuum region is represented by the largest number. The criterion used to choose individual thicknesses is the following: A light ray propagated at a tilt angle $\Psi_{\rm obs}=0°$ must pass through at least 95% of the model.

Once the two-slice model is constructed, the left-hand side of Eqs. (20) and (22) are known quantities and the two time ratios $(t_{\rm out}/t_{\rm in})_F$ and $(t_{\rm out}/t_{\rm in})_K$ can be determined. In an Einstein–de Sitter slice, this ratio is known analytically through Eq. (69) and, for time-reversed rays, $(t_{\rm out}/t_{\rm in})\leqslant 1$ since $(z_{\rm out}-z_{\rm in})\leqslant 0$. In the observer's slice initial conditions must be used for $t_{\rm in}\equiv t_{\rm obs}$, $\Psi_{\rm in}\equiv\Psi_{\rm obs}$, and $z_{\rm in}\equiv z_{\rm obs}\equiv 0$. In the first Kasner slice (i.e., the second slab of the model) $t_{\rm out}/t_{\rm in}$ is known analytically, via relation (70), only if $\Psi_{\rm obs}=0°$, whereas in cases for which $\Psi_{\rm obs}\neq 0°$, the time ratio must be determined numerically. The upper bound of the integral described by Eq. (22) must be changed until the right-hand side of the same relation is equal to $b(Z_{\rm out}-Z_{\rm in})_K$, inside a preset tolerance range. Once a proper value for $t_{\rm out}/t_{\rm in}$ has been ascertained, the radial distance traveled in the current Kasner slice can be evaluated by the direct numerical integration of relation (21).

For two-slice models with a proportionally much larger Kasner slice, the redshift factor for the entire model is overwhelmed by the Kasner contribution. The behavior of both x and Ψ versus time ratio is almost identical to Figs. 3(a) and 3(b), respectively.

Several graphs of key properties are provided in Fig. 4 (left).[7] The anisotropic nature of the vacuum region is clearly visible in the strikingly different behavior of C_+ and C_-. Furthermore, C_+ is much smaller than its Einstein–de Sitter counterpart, except in circumstances for which $(t/t_{\rm obs})$ approaches zero. Hence, the cross-sectional area $A\propto C_+C_-$ and the distortion factor, computed using C_+/C_-, will be highly affected. Also, note that the maximum value of A has moved to smaller $(t/t_{\rm obs})$.

The minimum point of $(C_+)_K$ can be found by setting $dC_+/dT=0$ in Eq. (61). When $(T/t_{\rm in})=\tan\Psi_{\rm in}/\sqrt{2}$, $(C_+)_K$ will have reached its minimum value. Since we are considering time-reversed beams, $\Psi_{\rm in}$ must satisfy $\tan(\Psi_{\rm in})_{\rm max}=\sqrt{2}$ so that a turnover may occur [i.e., if $\Psi_{\rm in}\geqslant 54.7°$ then $(C_+)_K$ can only increase].

Plots in Fig. 5 (left) offer a different view of two important characteristics of the beam: x and A. Both quantities are plotted versus the fractional distance traveled by the beam in the z direction. By definition, a fractional distance of 1 is reached by a beam with $\Psi_{\rm obs}=0°$; the larger the initial tilt

[7]From now on, we will use $t/t_{\rm obs}$ to denote the time ratio regardless of the space-time describing the current slice.

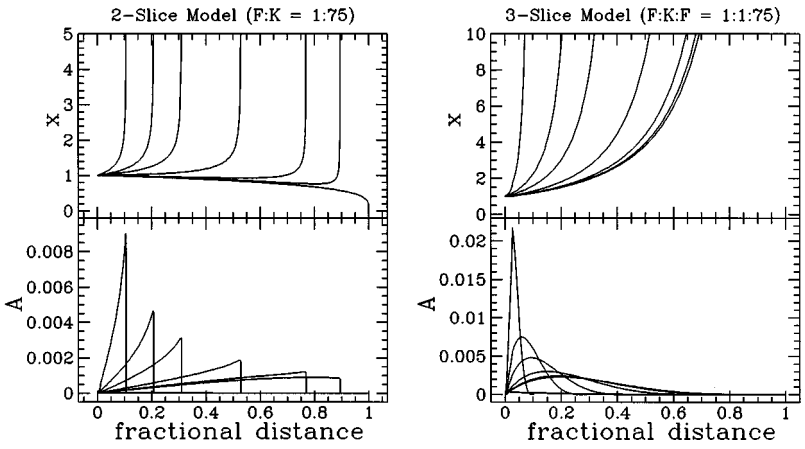

FIG. 5. Two- and three-slice models: x and A versus the fractional distance traveled across each model. A fractional distance of 1 is reached by a beam with $\Psi_{obs}=0°$, while the smallest fractional distance is reached by a beam with the largest angle, that is $\Psi_{obs}=80°$.

angle, the smaller the fractional distance will be once $(t/t_{obs})=0$ is reached.

2. Three-slice model

The purpose of the three-slice model is to isolate the effect of the Einstein–de Sitter space-time on the characteristics of the beam once shearing effects have been introduced. We have chosen the relative ''thicknesses'' to be in the proportion $F:K:F=1:1:75$, where the slice of interest is represented by the largest number.

The time ratio at any point in the third slice may be computed via relation (69), which enables us to calculate, through Eq. (19), the distance traveled in the radial direction. Equations (59) and (68) provide the principal curvatures of the wavefront in cases for which $\Psi_{obs}\neq 0°$ and $\Psi_{obs}=0°$, respectively. Pertinent plots are provided in Figs. 4 (right) and 5 (right).

All curves representing properties of the beam which do not involve C_+ are very close to the reference model, whichever Ψ_{obs} is used. Through the behavior of C_+, it is clear that the intervening Kasner slice, however small, will cause drastic changes in the cross-sectional area of the beam. Finally, note that the peak value of A has now moved to larger (t/t_{obs}).

For comparison purposes, we have included Fig. 6, which summarizes the properties of a beam propagated through a three-slice model with slabs of relative thicknesses in the proportion $F:K:F=1:1:13$. From the plots of A and C_+/C_- we know that, in the sampled range of Ψ_{obs} used, only beams for which $\Psi_{obs}=0°-40°$ were able to reach the third slab, while the three most tilted beams ended their journey in the Kasner region.

We want to emphasize the importance of the thickness of the first slice on the amplitude and behavior of C_+, with obvious consequences on A and the distortion factor. The tidal effects introduced in the beam as soon as the first Kasner slice is entered will drastically reduce the ability of C_+ to reach high amplitudes (except in cases with $t/t_{obs}\rightarrow 0$). Since C_- lies perpendicular to the axis of symmetry, it is not as sensitive to variations in the thickness of the observer's slice.

It is also worth mentioning that all physical properties of a beam of light traveling through the cheese slice model are now known analytically. The only exception is the evaluation, in Kasner regions, of the time variable along the beam as a function of affine parameter.

As a final note to this section, we now state a special condition that must be fulfilled in order for Eqs. (59), (62), and (63) to be valid representations of the principal curvatures in Einstein–de Sitter (once shearing has been introduced) and Kasner slices, respectively. Because of the degenerate nature of the characteristics of a beam that is propagated along the axis of symmetry (i.e., $\Psi_{obs}=0$), we must require that a beam for which $\Psi_{obs}\neq 0$ *must not contain this axis*; that is, if δ is the beam opening angle in the radial direction, then $\Psi>\delta/2$.

The properties of complete multislice models are studied in the next section.

IV. RESULTS FOR MULTISLICE MODELS

We initially consider cheese slice models which are constructed with slabs of equal thickness or, more precisely, slabs for which the left-hand sides of Eqs. (20) and (22) are all equal. For all models, we evaluate the change in apparent magnitude of a source due to lensing: Δm. The corrected apparent magnitude of the source is [23]

$$m_c=M+25+5\log_{10}(c/H_{obs})+5\log_{10}(D_L)\equiv m_F+\Delta m, \tag{71}$$

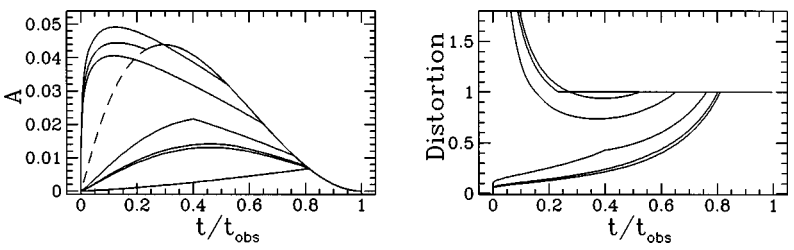

FIG. 6. Three-slice model with $F:K:F=1:1:13$. Note that the curves with the smallest Ψ_{obs} will break away from the reference curves at the largest (t/t_{obs}).

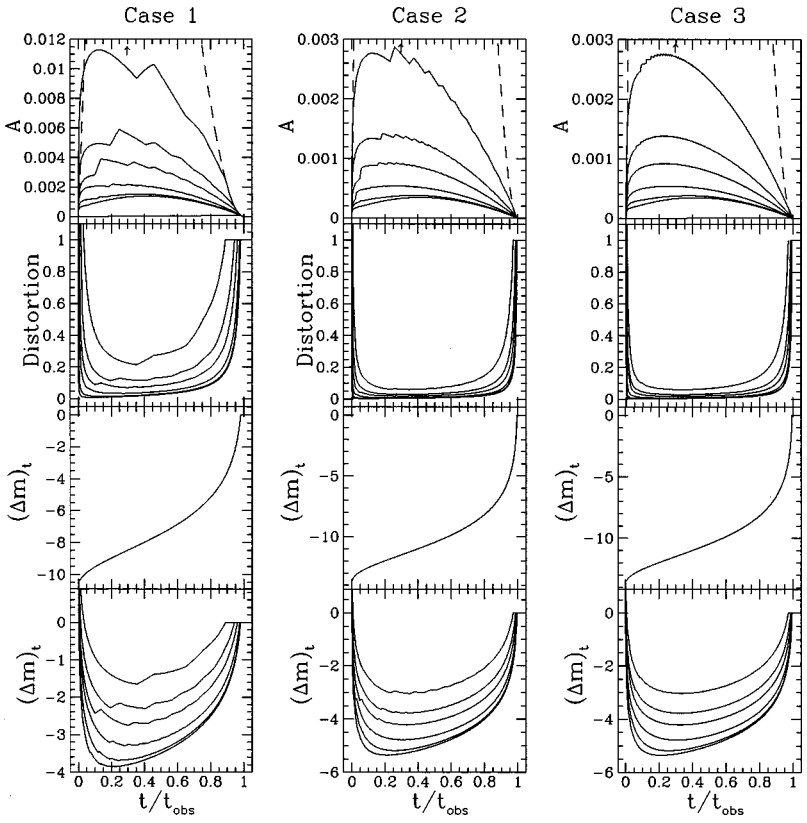

FIG. 7. Multislice models: The 50- and 200-slice models (cases 1 and 2) are constructed with slices of equal thickness, while in the 2000-slice model (case 3) all slices but the first are of equal thickness (see text for more details). For all plots, as for their counterparts in Fig. 4 we have used the same parameters in the same sequence. $(\Delta m)_t$ was evaluated using $\Psi_{\rm obs}=0°$ (upper graph) and, for the lower graph, 10° (bottom line) to 80° (top line).

where M is the absolute magnitude, $c/H_{\rm obs}$ is in megaparsecs, $D_L=(1+z)^2\sqrt{2A}$ is the luminosity distance in units of $(c/H_{\rm obs})$, m_F is the apparent magnitude the source would have in the reference universe, and $\Delta m=2.5\log_{10}(A/A_F)$.

Once a proper value for A has been determined, the corresponding cross-sectional area the beam would have in the absence of lensing is evaluated at the same redshift factor x, through Eq. (48), and the same time ratio $(t/t_{\rm obs})$, via relation (47). Thus, two distinct quantities are obtained: $(\Delta m)_x$ where both A and A_F are evaluated at the same redshift and $(\Delta m)_t$ where both A and A_F are evaluated at the same time ratio.[8] Again, we consider time-reversed beams, and so the use of $(\Delta m)_x$ is restricted to cases for which $x\geqslant 1$, since no blueshift effect can be obtained via the reference model.

The effects on the properties of a beam propagated through a 50-slice model (case 1) are presented first. Pertinent plots are provided in Figs. 7 and 8. For a given time ratio, the cross-sectional area of a beam traveling through the cheese slice model is smaller than its Einstein–de Sitter counterpart, except when $(t/t_{\rm obs})$ approaches 0. The resulting amplification of the source translates into a negative $(\Delta m)_t$ for all time ratios but $(t/t_{\rm obs})\rightarrow 0$. The unmistakable signatures of both space-times are clearly visible in the sharp variations of $(\Delta m)_x$ for small tilt angles and low redshifts. The amplification of the source is at its maximum near $x\sim 10^{0.4}\simeq 2.5$, which is quite close to the redshift factor at which A_F reaches its maximum value, that is, $x=2.25$. We remind the reader that in Kasner regions A peaks at comparatively smaller $(t/t_{\rm obs})$ and higher x.

Figures 7 and 8 also illustrate the properties of a beam traveling through a 200-slice model (case 2). The structure, strikingly visible in case 1, has been considerably smoothed out, even in cases for which $\Psi_{\rm obs}$ is large. Again, C_+ has been considerably reduced in magnitude. Thus, all curves representing A have been scaled down and the distortion effects enhanced. For a given $\Psi_{\rm obs}$, the correction to the apparent magnitude $(\Delta m)_t$ needed to account for the lensing effects is now larger (i.e., more negative), although the shape of the curves is similar to the shape of those found for case 1.

In order to isolate the effects of increasing the number of slices on the propagation of the beam, we now use a 2000-slice model (case 3) where the first slice is identical to its counterpart from the previous 200-slice construction (i.e., all slices but the first are of equal thickness). This will enable C_+ to reach the same amplitude at exit of the first slab, and any changes in the characteristics of the beam will be due solely to the now thinner and more numerous slabs. The only perceivable consequence of a tenfold increase in the number of slices is to almost completely eliminate any irregularities in the curves (see Figs. 7 and 8). A further augmentation, say, by a factor of 5, would totally hide the identity of individual slices; that is, as long as the observer's slice remains unchanged, we could not tell in which space-time the beam is traveling into at a given $(t/t_{\rm obs})$ by simply looking at the plots.

Finally, a 2000-slice model was constructed using the

[8]Note that both A and A_F are in units of $(c/H_{\rm obs})^2$. If one wishes to use a different value for $H_{\rm obs}$ in the reference model, a proper rescaling of all Δm curves will have to be made.

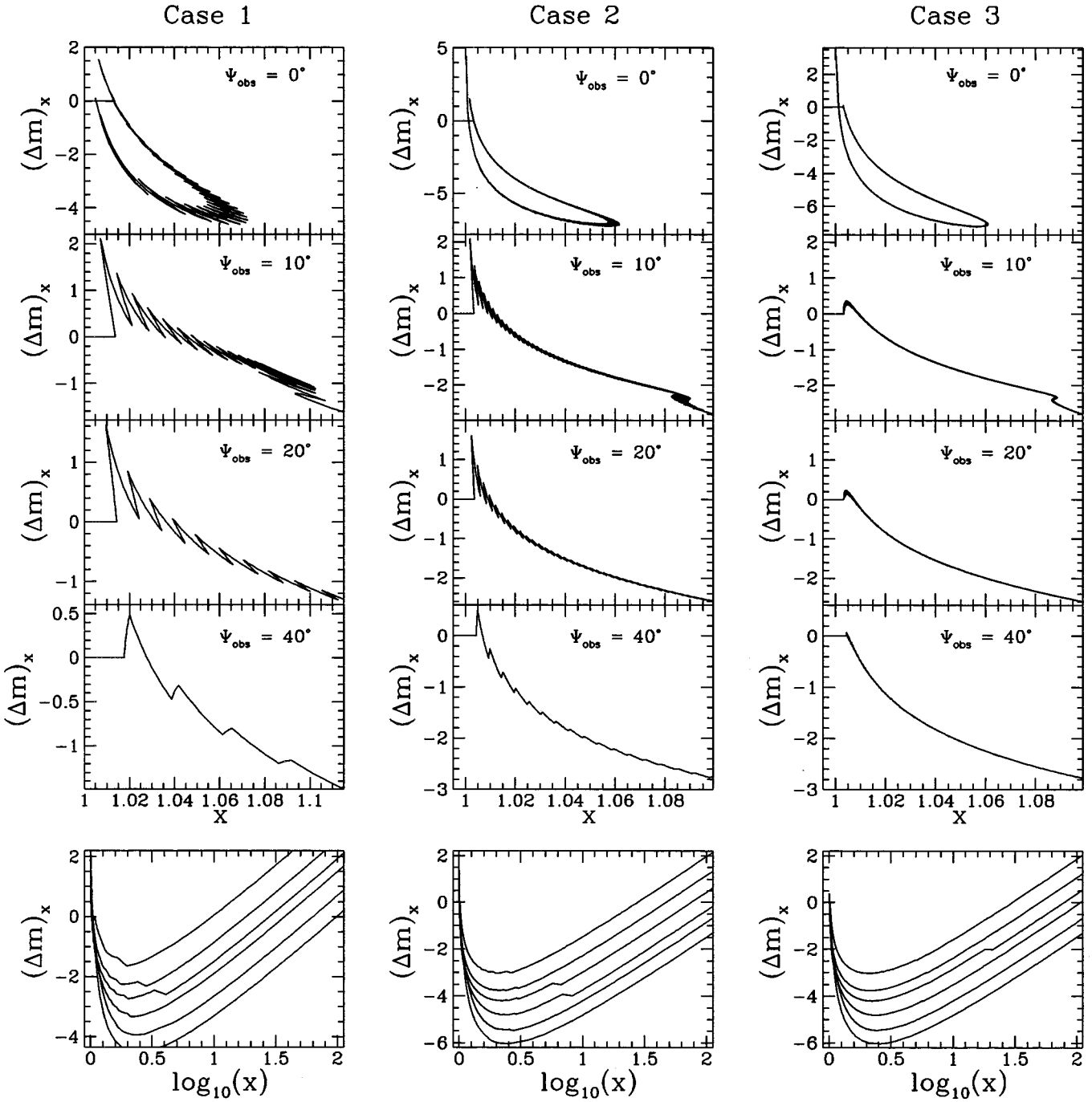

FIG. 8. Multislice models: $(\Delta m)_x$ versus x and $\log_{10}(x)$. Bottom graphs: $(\Delta m)_x$ was computed using $\Psi_{obs}=10°$ (bottom line) to 80° (top line).

same observer's slice and 1999 randomly selected slab thicknesses. In order to generate the sample, 1998 random numbers between 0 and 1 were produced and sorted. The relative thicknesses were computed by the subtraction of two neighboring numbers, and a scaling factor, representative of the total thickness desired, was used to calculate the final thickness for each slab. This simple method ensured that no overly large or small slabs were part of the sample. Slight differences were noticeable at large Ψ_{obs} for C_+ and A, whereas $(\Delta m)_x$ differed from the previous model at low redshift and small Ψ_{obs}. However, if the number of slabs between the observer and the source is expected to be large, say, larger then a few thousands, there appears to be no incentive to warrant the use of random over equal-slice models.

From the observer's point of view, the look-back time is not a suitable choice of independent variable, and thus the redshift factor is used in all remaining plots. Graphs of the angular size distance $D_<$, the luminosity distance $D_L=(1+z)^2 D_<$, and the axial ratio ($\equiv$ distortion factor $\propto C_+/C_-$) as functions of redshift factor are provided in Figs. 9 and 10 for various $\Psi_{obs}\pm\delta\Psi_{obs}$. Each graph contains five curves which illustrate the variations in the results caused by a slight change in the direction of observation. In

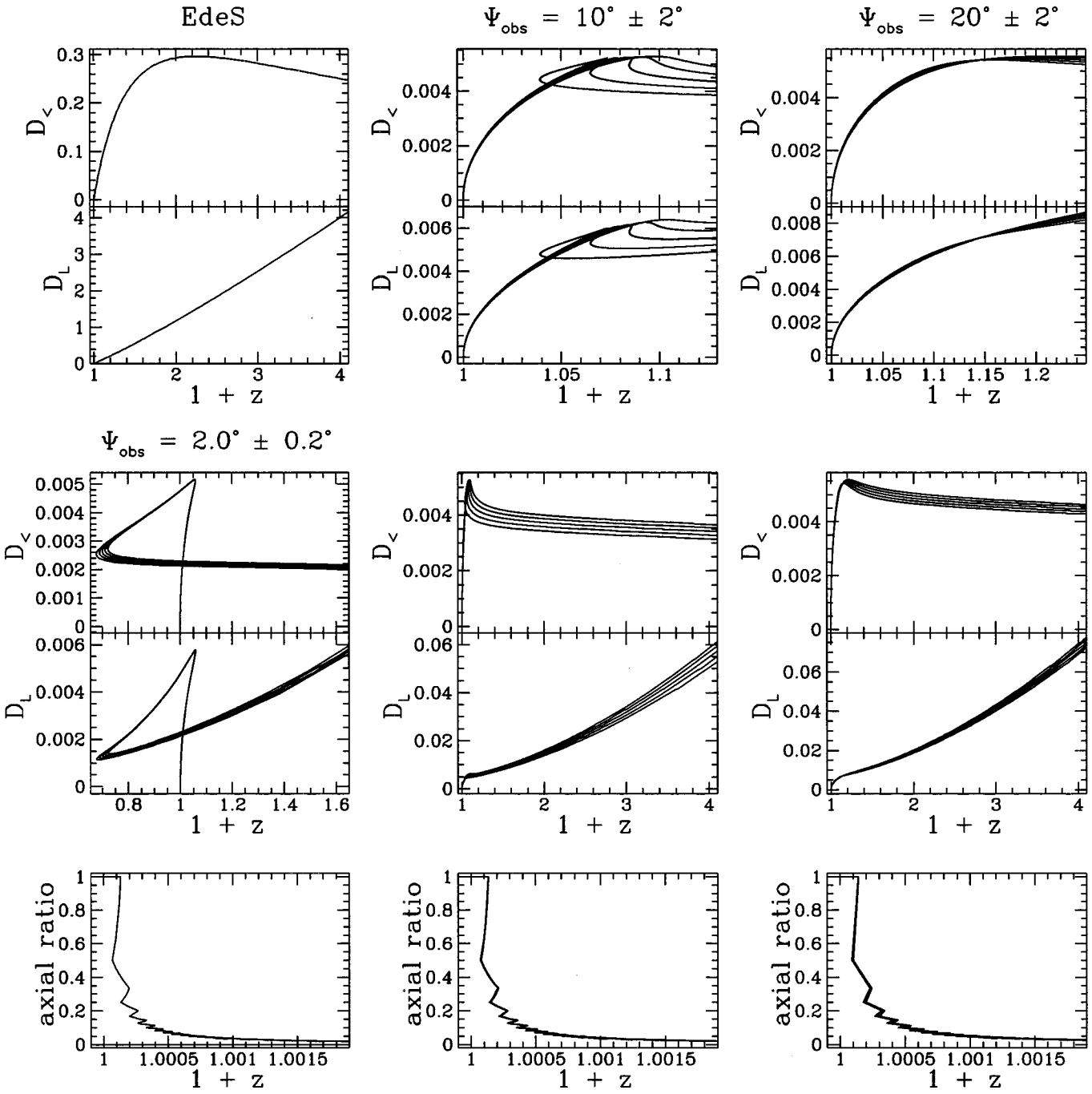

FIG. 9. In the Einstein–de Sitter cosmology (EdeS), $D_<$ reaches peak value at $x \equiv 1+z = 2.25$. $\Psi_{obs} = 2° \pm 0.2°$ graphs: observational tests for $\Psi_{obs} = 1.8°$ (bottom curve or curve that reaches lowest x value), 1.9°, 2.0°, 2.1°, and 2.2° (top curve). The maximum value of $D_<$ is now much lower and near $x \simeq 1.05$. Since shearing effects are introduced in the beam early on, the image of the source will be highly deformed even at very low redshifts. $\Psi_{obs} = 10° \pm 2°$ graphs: observational tests for $\Psi_{obs} = 8°$ (bottom curve), 9°, 10°, 11°, and 12° (top curve). The peak value of $D_<$ is now located in a broader range of x: $1.07 < x < 1.1$. $\Psi_{obs} = 20° \pm 2°$: observational tests for $\Psi_{obs} = 18°$ (bottom curve), 19°, 20°, 21°, and 22° (top curve).

all cases but $\Psi_{obs} = 2°$, redshift factors up to 4 were considered. Both $D_<$ and D_L are expressed in units of (c/H_{obs}), whereas the axial ratio is dimensionless. A 5000-slice model constructed with slabs of equal thickness was used to produce the results. The cross-sectional area of the beam is chosen to be initially circular; i.e., it is assumed that on average the image of the source is circular if no lensing occurs.

The behavior of $D_<$ and D_L for small Ψ_{obs} is somewhat complex since overall blueshift effects are possible (see Fig. 9), and both functions can take more than one value at a given x, whereas $D_<$ and D_L evaluated for larger Ψ_{obs} are considerably reduced in amplitude but similar in shape to

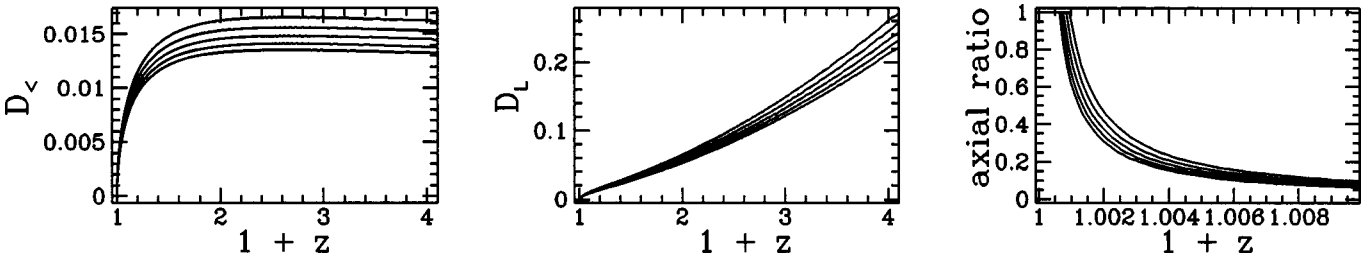

FIG. 10. 5000-slice model: observational tests for $\Psi_{obs} = 80° \pm 2.0°$.

their Einstein–de Sitter counterparts. Hence, considerable amplification effects are expected; i.e., the source appears brighter than it would in the absence of lensing.

For all Ψ_{obs}, the image ellipticity increases sharply with x (i.e., the axial ratio decreases) as soon as tidal distortions are introduced in the beam. The distribution of ellipticities about the axis of symmetry is quite spectacular. The minor axis of the cross-sectional area of the beam (C_+) always points towards the axis of symmetry, while the major axis (C_-) is tangential to the axis of symmetry and lies in a plane perpendicular to it. The alignment of all minor axes and the alignment of all major axes suggest a simple scheme to locate the direction of layering in the matter distribution. In addition, as Ψ_{obs} increases the redshift factor at which $D_<$ reaches its maximum value is shifted towards larger x, in most cases, the slope of D_L curves increases (i.e., the apparent brightness of a given source decreases as Ψ_{obs} increases), and in most cases, for redshift factors larger than at peak value, a noticeable flattening of $D_<$ curves occurs.

If we were to use a cheese slice model with a different number of slabs, or one with a larger first slice, variations in the results would of course occur but the major trends discussed above would still apply.

V. CONCLUSIONS

The observational relations in a universe with density inhomogeneities extending over the largest distance scales have been studied in the exact case where the lensing is caused by large slabs of alternating pure vacuum and dust. Significant bending and anisotropic redshift effects are introduced in the beam. It is clear that the introduction of such large inhomogeneous structures can have dramatic effects on the physical properties of a bundle of rays.

In all multislice models considered, the action of the tidal forces on the beam results in a peculiar distribution of ellipticities about the axis of symmetry of the model. This alignment pattern does not seem to agree with observations, although an apparent layering in the distribution of galaxies was reported by several authors, as discussed in the Introduction. Furthermore, the image axial ratio decreases sharply with redshift as soon as shear is introduced in the beam (i.e., as soon as the first Kasner slab is crossed). In fact, if one wishes to retrieve the Einstein–de Sitter space-time, the source must be located in the observer's slice (i.e., one must extend the observer's slice to include the entire observable universe).

The systematic and direction-dependent distortion of distant images is of particular interest. This distortion has the same radial compression and tangential stretching familiar with the more conventional gravitational lens effects of galaxies or clusters of galaxies. In our case, this distortion arises from a uniformly thick slab of matter, while in the conventional situation, where the gravitational lensing effects are simply overlaid on the background FLRW universe, the uniformly thick slab introduces no distortion.

The cheese slice model displays strong inhomogeneity while remaining dynamically self-consistent. This differs strongly from the more usual calculations of observational effects in superposition models of inhomogeneity, such as have been used by many authors (for instance, see Ref. [24] and references therein). These approaches suffer from problems of internal inconsistencies, since it is not possible to overlay an arbitrary inhomogeneity on the background FLRW model without destroying the important properties of the FLRW model itself.

It is well known that to preserve the foundations of the FLRW model, one can only insert spherically symmetric, mass-compensating, matter distributions, of which the classical Swiss cheese vacuole model is the extreme limit, and the rest of which can be described by the Bondi-Tolman solutions and their generalizations. For the case of spatially bounded inhomogeneous structures, there is always the hope that averaging over a sufficiently large scale will recover some of the FLRW properties, since the ''mass excess'' (and thus the Weyl curvature representing the tidal effects) may be relatively diminished in well chosen cases.

The possibility of averaging over sufficiently large scales in order to diminish the influence of a given quasispherical inhomogeneity does not present itself for topologically open structures like large sheets, for a number of reasons. In the case at hand, there will not exist any distance scale over which the effects discussed above can be made to relatively vanish. This significantly changes the approach that must be taken, and in particular it means that the requirement for self-consistency cannot be ignored quite so easily as in the quasispherical case. It now becomes very important that the dynamics of the constituents of the model universe remain consistent over large times rather than just over short periods.

The present work has been restricted to the consideration of a single parallel family of slicings in the universe. The planar symmetry inherent to the cheese slice matter distribution causes the action of the tidal forces to be highly directional. In order to eliminate such a preferred direction, future work should consider the case where there are three sets of mutually orthogonal slicings so that one may fully model a

lattice universe. Consideration of this case is in progress, but there are significant difficulties in finding appropriate solutions to the Einstein field equations. Nevertheless, the cheese slice model provides new and interesting results since it is one of the rare attempts at studying the effects of very large scale inhomogeneities on the propagation of light beams.

ACKNOWLEDGMENTS

The authors are grateful to J. F. Harper for helpful discussions. Financial support was provided in part by the Natural Sciences and Engineering Research Council of Canada and the Kappa Kappa Gamma Foundation of Canada.

[1] V. de Lapparent, M. J. Geller, and J. P. Huchra, Astrophys. J. **302**, L1 (1986).
[2] A. Dressler, S. M. Faber, D. Burstein, R. L. Davies, D. Lynden-Bell, R. J. Terlevich, and G. Wegner, Astrophys. J. **313**, L37 (1987).
[3] S. Refsdal, Astrophys. J. **159**, 357 (1970).
[4] C. C. Dyer and R. C. Roeder, Astrophys. J. **174**, L115 (1972).
[5] C. C. Dyer and R. C. Roeder, Astrophys. J. **180**, L31 (1973).
[6] C. C. Dyer and R. C. Roeder, Astrophys. J. **189**, 167 (1974).
[7] R. R. Bourassa and R. Kantowski, Astrophys. J. **205**, 674 (1976).
[8] C. Alcock and N. Anderson, Astrophys. J. **302**, 43 (1986).
[9] J. A. Peacock, Mon. Not. R. Astron. Soc. **223**, 113 (1986).
[10] K. Watanabe and K. Tomita, Astrophys. J. **355**, 1 (1990).
[11] J. F. Harper, Ph.D. thesis, University of Toronto, 1991.
[12] T. J. Broadhurst, R. S. Ellis, D. C. Koo, and A. S. Szalay, Nature (London) **343**, 726 (1990).
[13] G. R. Burbidge and E. M. Burbidge, Astrophys. J. **148**, L107 (1967).
[14] H. Arp, H. G. Bi, Y. Chu, and X. Zhu, Astron. Astrophys. **239**, 33 (1990).
[15] B. Lehle, ''Optical Properties of Ultra-Large Scale Structure in the Universe,'' Senior Project Report: Department of Astronomy, University of Toronto, 1992.
[16] W. B. Bonnor and P. A. Vickers, Gen. Relativ. Gravit. **13**, 29 (1981).
[17] C. C. Dyer, S. Landry, and E. G. Shaver, Phys. Rev. D **47**, 1404 (1993).
[18] R. Sachs, Proc. R. Soc. London **A264**, 309 (1961).
[19] R. Kantowski, J. Math. Phys. (N.Y.) **9**, 336 (1968).
[20] C. C. Dyer, Ph.D. thesis, University of Toronto, 1973.
[21] F. A. E. Pirani, *Brandeis Lecture on General Relativity* (Prentice-Hall, Englewood Cliffs, NJ, 1964), p. 337.
[22] E. Kreyszig, *Advanced Engineering Mathematics* (Wiley, New York, 1983), p. 100.
[23] G. C. McVittie, *General Relativity and Cosmology* (University of Illinois Press, Urbana, 1965), p. 174.
[24] K. Tomita, Prog. Theor. Phys. **85**, 57 (1991).